# Electric fields, cloud microphysics, and reflectivity in anvils of Florida thunderstorms

J. E. Dye,[1] M. G. Bateman,[2] H. J. Christian,[3] E. Defer,[4] C. A. Grainger,[5] W. D. Hall,[1]
E. P. Krider,[6] S. A. Lewis,[7] D. M. Mach,[3] F. J. Merceret,[8] J. C. Willett,[9]
and P. T. Willis[10]

[1] A coordinated aircraft–radar project that investigated the electric fields, cloud microphysics, and radar reflectivity of thunderstorm anvils near Kennedy Space Center is described. Measurements from two cases illustrate the extensive nature of the microphysics and electric field observations. As the aircraft flew from the edges of anvils into the interior, electric fields very frequently increased abruptly from $\sim$1 to >10 kV m$^1$ even though the particle concentrations and radar reflectivity increased smoothly. The abrupt increase in field usually occurred when the aircraft entered regions with a reflectivity of 10–15 dBZ. We suggest that the abrupt increase in electric field was because the charge advection from the convective core did not occur across the entire breadth of the anvil and because the advection of charge was not constant in time. Also, some long-lived anvils showed enhancement of electric field and reflectivity far downwind of the convective core. Screening layers were not detected near the edges of the anvils. Comparisons of electric field magnitude with particle concentration or reflectivity for a combined data set that included all anvil measurements showed a threshold behavior. When the average reflectivity, such as in a 3-km cube, was less than approximately 5 dBZ, the electric field magnitude was <3 kV m$^1$. Based on these findings, the Volume Averaged Height Integrated Radar Reflectivity (VAHIRR) is now being used by the NASA, the Air Force, the and Federal Aviation Administration in new Lightning Launch Commit Criteria as a diagnostic for high electric fields in anvils.

## 1. Introduction

[2] Numerous studies have investigated the microphysical conditions and radar reflectivity structure of convective clouds when charge separation is beginning and electric fields are intensifying, but few studies have examined the decay of electric fields in space and/or time in thunderstorm anvils as a function of the cloud microphysics and radar reflectivity. Since thunderstorm anvils can contain high electric fields, they pose a significant threat for triggering

lightning during space flight operations. Until recently the mission launch rules at the National Aeronautics and Space Administration (NASA) Kennedy Space Center (KSC) and the Air Force Eastern Range would prevent a space vehicle from flying through nontransparent anvils or even an anvil detached from the parent convection if lightning had occurred within the last 3 hours in the parent storm or the anvil [*Krider et al.*, 1999].

[3] The Airborne Field Mill II experiment (ABFM II) was conducted near KSC to measure the electric field, reflectivity, and microphysics in thunderstorm anvils (and other clouds) produced by deep convection with the hope that the launch constraints involving anvil clouds could be safely relaxed. In this paper, we present a brief overview of the ABFM II campaigns, examples of some of the measurements, and a synthesis of the results obtained in 14 different flights through anvils. During the analysis of ABFM II observations and while attempting to compare the observations with estimates of electric field decay predicted from a simple model [*Willett and Dye*, 2003], we found that reflectivity and strong electric fields persisted and became uniform in a stratiform-like mid-level layer for many tens of minutes over many tens of kilometers well downstream of the parent convection. This "enhancement" of reflectivity,

[1]National Center for Atmospheric Research, Boulder, Colorado, USA.
[2]Universities Space Research Association, Huntsville, Alabama, USA.
[3]University of Alabama in Huntsville, Huntsville, Alabama, USA.
[4]Observatoire de Paris, Paris, France.
[5]University of North Dakota, Grand Forks, North Dakota, USA.
[6]University of Arizona, Tucson, Arizona, USA.
[7]NOAA/University of Colorado, Cooperative Institute for Research in Environmental Sciences, Boulder, Colorado, USA.
[8]National Aeronautics and Space Administration, Kennedy Space Center, Florida, USA.
[9]Garrett Park, Maryland, USA.
[10]NOAA Cooperative Institute for Marine and Atmospheric Sciences, Miami, FL, USA.

electric field, and microphysics in two long-lived anvils is discussed in a separate paper [*Dye and Willett*, 2007] that argues that weak updrafts were probably present and that charge separation must have occurred in these long-lived anvils. The simple model based on ABFM II particle observations, which was used to estimate the electric field decay in passive anvils and was compared with the electric field observations from ABFM II, will be described elsewhere.

## 2. The Airborne Field Mill Experiment

[4] The ABFM II campaigns were conducted during June 2000 and May–June 2001 to investigate the relationships between microphysics, radar reflectivity, and the decay of electric fields (both spatially and temporally) in thunderstorm anvils and other clouds. In situ measurements of the three-dimensional electric field, particle concentration, types, and sizes, and standard thermodynamic and flight measurements were made using a Citation II jet aircraft operated by the University of North Dakota (UND) (for information on the Citation and its instrumentation for ABFM II, see *Ward et al.* [2003]). The aircraft measurements were coordinated with reflectivity measurements by the WSR-74C radar at Patrick Air Force Base, Florida, and the NEXRAD WSR-88D radar at Melbourne, Florida. The occurrence and location of intracloud (IC) and cloud-to-ground (CG) lightning flashes were determined using the KSC Lightning Detection and Ranging (LDAR) system [*Lennon and Maier*, 1991] and the KSC Cloud-to-Ground Lightning Surveillance System (CGLSS) [*Maier*, 1991].

[5] The anvils ranged in size from small anvils of short-lived air mass thunderstorms to anvils formed by mid-level outflow to large anvils of intense multicellular, long-lived thunderstorms. Initial penetrations were often made across the anvil outflow close to the convective cores of the storms. Subsequent cross anvil passes were made at different distances downstream to examine the decay of the electric field with both time and distance. Some passes were also made along the axis of the anvil outflow either toward or away from the core of the storm.

[6] Aircraft penetrations were typically made at altitudes ranging from 7 to 11 km mean sea level (MSL) [−15 to −45°C], with 80% of the penetrations made at 8–10 km MSL (about −20 to −35°C) and mostly near 9 km MSL (approximately −31 to −32°C), because the middle of the anvil was usually at these altitudes (hereafter all altitudes are referenced to mean sea level, MSL). Spiral ascents or descents were made through the anvils when Air Traffic Control (ATC) would allow, but these were relatively infrequent because of heavy airliner traffic in that region of Florida. In some cases, the aircraft arrived after most of the electric field had already decayed but these cases are also useful because we know the reflectivity history of these storms and the time of the last lightning relative to the aircraft penetrations. Decisions on where to fly were based on interactions between the air crew and ground coordinators at the Air Force Range Operations Control Center (ROCC), where aircraft track could be overlaid on vertical and horizontal cross-sections of the radar reflectivity and where displays of lightning, ground-based electric field, and satellite observations were available in real time.

[7] In the following subsections, we present a brief summary of instruments and measurement systems used during the project. More information on each of these measurement systems is given by *Dye et al.* [2004].

### 2.1. Airborne Measurement of Electric Field

[8] The three-dimensional electric field was measured in situ from the UND Citation using six low noise, high dynamic range, rotating-vane field mills that were designed and built at NASA Marshall Space Flight Center [*Bateman et al.*, 2006]. The use of two input channels with overlapping gains and 16-bit analog-to-digital converters permitted a measurement range from less than 1 V/m to 150 kV m$^{-1}$. The data were digitized inside each field mill close to the source so as to minimize electrical noise from the aircraft. The mills were time synchronized to within 16 ms of each other by a central data collection computer for the field mills, and the overall timing accuracy was within 50 ms of UTC. The data were recorded at 50 samples s$^{-1}$ but for this paper were averaged and plotted at 1 sample s$^{-1}$.

[9] When the aircraft was out of cloud, the charge on the aircraft was usually very small. Based on the analysis of *Mach and Koshak* [2003], we feel that the uncertainty in the measured electric field out of cloud was within ±10%. When the aircraft penetrated a cloud, however, the errors increased significantly because of aircraft charging. In this case, $E_z$ and $E_y$, the field components in the vertical and along the wings, respectively, were accurate to about 20%. The $E_x$ component along the fuselage was much less accurate. (We used a right-handed coordinate system with $E_z$ positive upward, $E_x$ positive forward, and a sign convention in the traditional physics sense, that is, a positive field shows the direction in which a positive charge would move. $E_x$, $E_y$, and $E_z$ are relative to the aircraft.) More details on the placement of the field mills on the aircraft, the techniques used to determine the three-dimensional electric field, and the calibration of the system is given by *Mach and Koshak* [2003] and by *Dye et al.* [2004, Appendix B].

### 2.2. Airborne Microphysical Measurements

[10] Five separate microphysical instruments were flown on the Citation to determine the concentration, sizes, and types of particles ranging from a few microns to about 5 cm, thus covering a range from frozen cloud droplets to large aggregates. Descriptions of all instruments used are available in the literature. Herein we cite only recent publications for each instrument that discuss the measurement techniques, sources of measurement error, and that include references to earlier published studies. A Particle Measuring Systems (PMS) Forward Scattering Spectrometer Probe (FSSP) was used for the size range of a few microns to ~50 μm. The FSSP was designed to measure water droplets and has shortcomings in ice and mixed phase clouds [*Field et al.*, 2003]. We used the FSSP only as an indication of the relative concentration of the small ice particles. A PMS two-dimensional cloud probe (2D-C) [*Strapp et al.*, 2001; *Field et al.*, 2006] nominally covered the range of 30 μm to a few millimeters and gave shadow images of the particles from which information on particle type can be obtained as well as the size and concentration. A PMS one-dimensional cloud probe (1D-C), which is similar to the 2D-C but does not image the particles, gave measurements of the concen-

tration of particles in 15 size bins from 15 to 960 $\mu$m. A Stratton Park Engineering Corp (SPEC) Cloud Particle Imager (CPI) [*Lawson et al.*, 2001] provided images of particles with resolution of 2.5 $\mu$m over its effective size range of ~10 $\mu$m to about 2 mm, with images of the larger sizes limited by the small sample volume. Measurements from the CPI were used only to examine particle type. The SPEC High Volume Particle Sensor (HVPS) [*Lawson et al.*, 1998] images particles in the nominal range of 1 mm to 5 cm with a resolution of 400 $\mu$m along the direction of flight and 200 $\mu$m in the cross stream direction. Like the 2D-C, special software is needed to process the data and to determine the concentration in different size ranges. We used software developed at NCAR for processing and displaying the ABFM II microphysical measurements. In general, the cloud physics instruments worked well and normally there was very good agreement in the overlap regions between different probes.

[11] Assigning an uncertainty to the concentration and size measurements from each instrument is not straightforward. The concentration, $n_i$, in any size interval, $i$, measured by these instruments is $C_i/v_i$, where $C_i$ and $v_i$ are the number of counts and sample volume in that size interval. The statistical uncertainty of the measured concentration in that size bin is then approximately $(\sqrt{C_i})/v_i$. The number of counts in the size bins of each instrument is dependent upon the integration time and the relative abundance of particles. In ABFM II for 10-s averaging periods, in the small/ intermediate-sized intervals we typically counted many tens or hundreds of particles, whereas for the larger size bins of each instrument the number of counts was typically only a few particles. Thus there is little statistical uncertainty (<10%) for the small to mid size range measured by each instrument and a factor of 2 or more uncertainty for the largest sizes. Because of the overlap between the 2D-C and the HVPS for the millimeter-sized particles, the statistical uncertainty of the composite size distributions in this overlap region is probably <30%, when both instruments are functioning well. Errors in sizing for these instruments are greatest when the particle size becomes comparable to the spacing between the diode elements [see *Strapp et al.*, 2001] and when the particles are larger than or near the size of the full width of the diode array. For the 2D-C flown on the Citation, this width is roughly 1 mm. In the middle of the size range of each instrument, sizing errors are probably <15%.

[12] In addition, to the particle probes the Citation carried a King liquid water sensor and a Rosemount Icing Detector [*Heymsfield and Milosevich*, 1989]. The measurements from the King liquid water sensor were rarely used in our ABFM II analyses because we flew mostly in anvils and other cloud regions that contained primarily ice particles. The icing detector was a valuable instrument that allowed us to determine when supercooled liquid water was present in our clouds. Analysis of the icing detector measurements by *Schild* [2003] and other unpublished undergraduate work at UND showed no evidence of supercooled water in the ABFM II anvils, so all particles discussed in this paper are considered to be ice.

## 2.3. Radar Reflectivity Measurements

[13] Radar measurements were obtained from a WSR-74C (74C) radar located at Patrick Air Force Base (about 25 km south of KSC) and the WSR-88D (88D) NEXRAD radar located at Melbourne, Florida, about 18 km to the southwest of the 74C radar. (The location of the 74C radar was used as the origin in all of our radar plots.) The 74C radar provides support for all launch operations at KSC and the Air Force Eastern Range. The 74C is a C-band (5.3 cm), horizontally polarized weather radar without Doppler capability. The peak power was 250 kW with a pulse repetition frequency (PRF) of 160 Hz. The beam width was 1.05° and the pulse width was 4 $\mu$s. It had a maximum range of 256 km with a range resolution of 250 m. Measurements were made during antenna ascent and descent with 12 interleaved 360° sweeps. A complete volume scan was made every 2.5 min.

[14] The NEXRAD 88D is an S-band 10 cm circularly polarized, Doppler weather radar. The beam width was 0.95°, the pulse width was 1.57 or 4.7 $\mu$s, and the peak power was 750 kW. The PRF varied from 318 to 1304 Hz. Pulse pair processing was used to recover the Doppler information. The normal range was 230 km, but degraded reflectivity data could be obtained at ranges as far as 460 km. A complete volume scan took 5–6 min. All ABFM II measurements were from the Volume Coverage Pattern precipitation-mode scan strategy, VCP 11 [*Office of the Federal Coordinator for Meteorology (OFCM)*, 2003].

[15] The universal format data from both radars were converted to a Cartesian 1-km grid with a 1-km horizontal and vertical spacing over a 225 × 225 km domain using SPRINT [*Mohr et al.*, 1986]. SPRINT was configured to perform a bilinear interpolation with a maximum acceptable distance of 0.2 km to relocate a closest point estimate and with no range interpolation. The reflectivity was converted from decibels to a linear scale for interpolation. Subjective comparisons of horizontal and vertical cross-sections of the 74C and 88D data sets showed good agreement when attenuation of the 74C was not a factor. Additionally, statistical tests were done for a limited set of quantitative reflectivity comparisons, and these tests found that the systematic differences (without attenuation) were less than 1 dBZ when examined over volumes of several tens of km$^3$.

[16] Attenuation of the 74C measured reflectivity was apparent behind regions of heavy precipitation or when the radome of the 74C was wetted because of precipitation. The 74C observations were manually checked for each flight to determine times when attenuation had occurred. For the analyses presented in Section 4 below NEXRAD data were substituted for the 74C data when 74C attenuation occurred for an individual case. Both radars have a cone of silence directly above the radar that was not scanned because it lies at an elevation angle higher than the elevation of the highest sweep angle. At an anvil altitude of 9 km, this corresponded to a horizontal diameter of ~20 km for the 74C and ~30 km for the 88D radars. The airborne data set that is used in Section 4 was carefully edited, so that it did not include data points when the anvil was in the cone of silence of the appropriate radar.

[17] When the difference between adjacent elevation sweeps exceeded the beam width of that radar, scan gaps occurred, that is, the radar did not completely sample the entire volume of radar space. These gaps produced a ragged appearance of the anvil tops, bases, and sides in the cross-sectional displays of the reflectivity measurements, particularly for storms far from the radar. The effects of radar

propagation can also cause the actual altitude to differ from the indicated altitude by a couple of kilometers [*Wheeler*, 1997]. These issues could present a problem when trying to compare the airborne measurements with the radar reflectivity measurements from the $1 \times 1 \times 1$ km gridded data. Some of the grid points can be in a scan gap and there can also be propagation effects. Constant Altitude Plan Position Indicator (CAPPI) plots and vertical sections along the aircraft tracks that are presented in this paper were based on the 1-km gridded radar data, so they sometimes display the artifacts. However, when airborne measurements of electric field or particle concentrations are plotted versus the radar reflectivity in Section 4 below, the 1-km gridded reflectivity data were averaged in dBZ over a 3-km cube in order to mitigate the effects of scan gaps and propagation effects. Pixels with no detectable return were not included in the averages, and we required that 16 of the 27 pixels in a 3-km cube contain measurable reflectivity.

## 2.4. Lightning Measurements

[18] Two lightning detection systems were used during ABFM II to determine occurrence, location, and frequency of lightning discharges. The Lightning Detection and Ranging (LDAR) system, which is a total lightning system using time-of-arrival techniques, located the sources of VHF radiation from lightning from 63 to 69 MHz [*Lennon and Maier*, 1991]. It consisted of a central site and six remote sensors that were approximately 10 km radius from the central site. Studies by *Boccippio et al.* [2000a, 2000b] show that the flash detection efficiency is >90% within 100 km range and <25% at 200 km range. The VHF source location error distribution is a function of range with a mean horizontal error of about 200 m at 100 km [see *Boccippio et al.*, 2000b, Figure 3]. For most of our analyses, we plotted the individual VHF sources overlaid on radar CAPPIs to show when and where lightning discharges occurred and have not separated the sources into flashes.

[19] The Cloud-to-Ground Lightning Surveillance System (CGLSS) provided the locations and times of cloud-to-ground (CG) return strokes [*Maier*, 1991]. During ABFM II, this system used six Global Atmospherics Inc. 141-T Advanced Lightning Direction-Finders operating over a wide bandwidth in and below the MF, an IMPACT 280-T Advanced Position Analyzer employing both radio-direction-finding and time-of-arrival techniques, and associated displays. The system was similar to the National Lightning Detection Network [*Cummins et al.*, 1998]. The sensors extended approximately 40 km to the north, west, and south of KSC. Within the perimeter of the network, the accuracy of location of CG strokes was about 300 m [*Boyd et al.*, 2005]. At a range of 100 km from the network the accuracy degraded to roughly 3 km. When all six sensors were functioning properly, the detection efficiency was better than 98%. More information on LDAR and CGLSS use in ABFM II are given by *Dye et al.* [2004, Appendices F and G].

## 3. Examples From Two Storms

[20] One of our first observations during ABFM II was that the transition from weak electric fields ($\sim$1 kV m$^1$) to thunderstorm strength fields ($\sim$10 kV m$^1$) in anvils was usually quite abrupt, and it occurred when the Citation flew from regions that had a reflectivity <10 dBZ into regions with greater reflectivity. Analysis also showed that the transition to strong fields was quite rapid in comparison to the more smoothly varying particle concentrations in all size ranges and radar reflectivity. Based on this finding by June 2001, the ground coordinators could often tell the aircraft crew where to expect large increases/decreases in electric fields based on the reflectivity display. In this section, we present two cases that illustrate the kinds and quality of the observations that were made during ABFM II and that also illustrate the abrupt increases in electric field.

### 3.1. 13 June 2000

[21] The 13 June storm was a long-lived storm with a well-developed anvil that was investigated by the Citation for over 3 hours from 2045 UTC to after 2400 UTC. (UTC is used throughout this paper; subtract four hours for local daylight time.) The Citation first entered the anvil when it was relatively small ($\sim$40 km length at 10 km altitude) but well defined. By 2200 the anvil at 10 km altitude, as deduced from radar observations, extended more than 100 km downwind of the original convective core. Penetrations were made from east to west or vice versa at $10-11$ km altitude across the anvil at $25-50$ km from the storm core from 2050 until 2225. After 2225 penetrations were made along or opposed to the direction of the wind along the axis of the anvil from southwest to northeast until $\sim$0005, first at 11 km altitude, then at 9 km, and finally at 8 km as the anvil subsided. In a separate paper, *Dye and Willett* [2007] used this case as well as the case of 4 June 2001 to illustrate the enhancement in reflectivity and electric field that was observed in some long-lived anvils. More information on the latter stages of the 13 June storm can be found in that paper.

[22] An example of an early cross anvil penetration from 2103 to 2111 is shown in Figure 1, as the Citation was climbing from 10 to 11 km. The reflectivity structure in the 10-km CAPPI reflects the downshear outflow and some upshear divergence from the upper level updraft. The maximum reflectivity in the storm at this time was $55-60$, $50-55$, and $40-45$ dBZ at 4, 7, and 10 km, respectively, but the reflectivity pattern of the core is obscured in Figure 1 by the red triangles showing the CG strokes. The CGLSS system showed that CG lightning occurred in the convective cores from 1915 until 2135. Because the LDAR system was not functioning properly in June 2000 until the following day, there is a paucity and mislocation of LDAR VHF sources in Figure 1.

[23] Comparison of the 10 and 4 km CAPPIs in Figure 1 shows that the anvil extended more than 50 km to the north, northeast of the main convection. There was some weak low-level convection north of the main core. The reflectivity curtain in the third panel of Figure 2 near $2109-2110$ shows precipitation falling to the ground in this region. From 2103 to 2108, the penetration was in the anvil that extended to the east. It is anvils such as this that have a well-defined base that are the focus of the studies described herein.

[24] Figure 2 shows a MER plot (microphysics, electric field, and reflectivity) for the 10-min period including the aircraft penetration shown in Figure 1. At the Citation typical flight speed of $\sim$120 m s$^{-1}$, 1 min corresponds to roughly 7 km of horizontal distance. The figure shows a
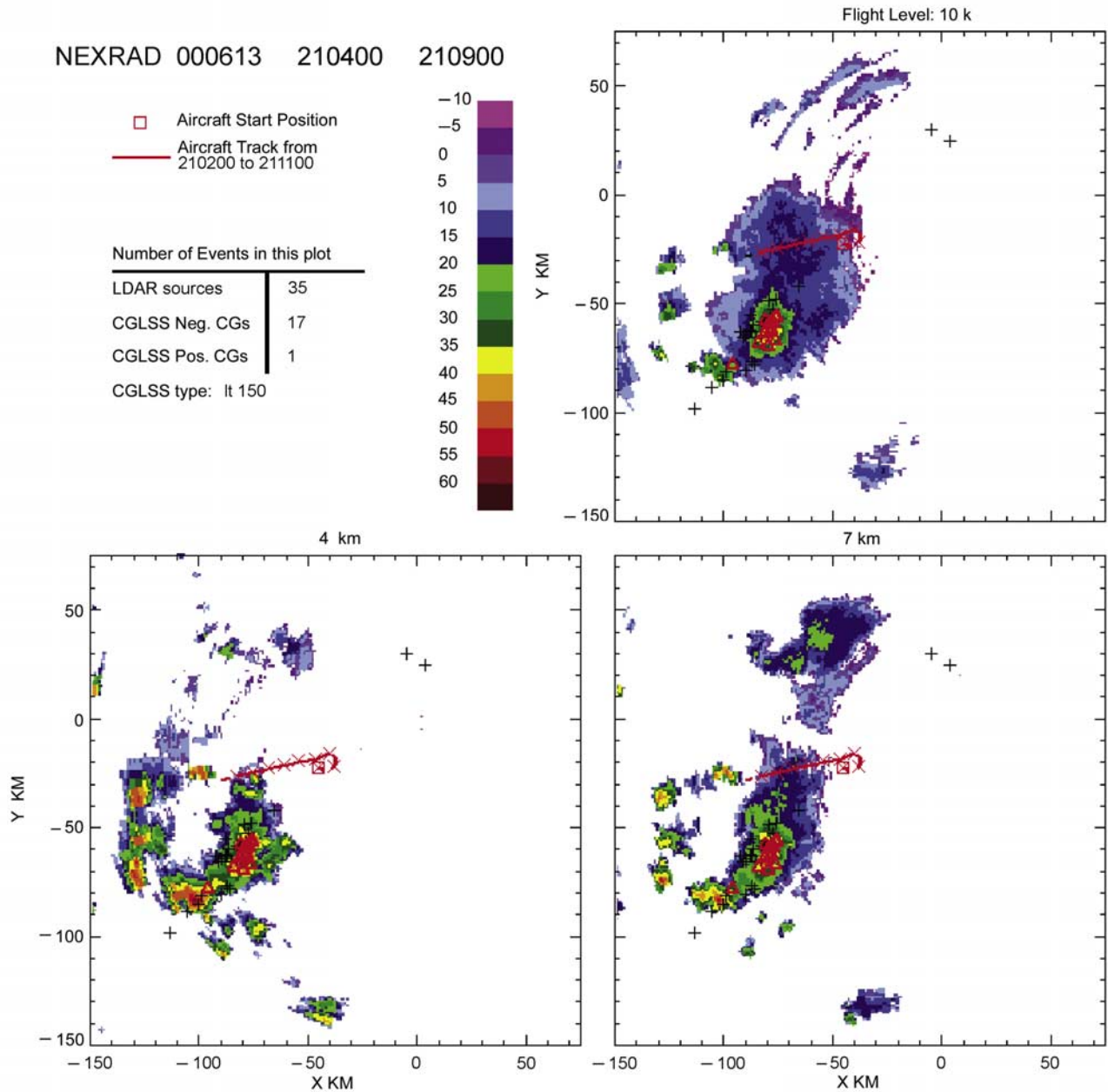
**Figure 1.** CAPPIs of reflectivity at 4, 7, and 10 km MSL for the 2104-2109 NEXRAD volume scan on 13 June 2000 with the Citation track from 2102 to 2111 overlaid in red. The initial position of the aircraft is shown by a square with Xs showing each successive minute along the track. Red triangles show the positions of CG flashes detected by the CGLSS system during this volume scan. The ground projection of LDAR VHF sources is shown by black pluses.

dramatic increase in electric field as the aircraft approached a reflectivity of about 15 dBZ near 2107. The scalar magnitude of the vector electric field, $E_{mag}$ (henceforth called the electric field magnitude), bottom panel in Figure 2, increased from ~3 to ~20 kV m$^{-1}$ in about 10 s (~1200 m). This large, rapid increase in field was a common feature of the ABFM II measurements. During this penetration, the field magnitude was dominated by $E_z$. Note that in the MER plots, $E_z$ is plotted on a linear scale shown on the left side of the figure, while the field magnitude, $E_{mag}$, is plotted on a log scale on the right side of the figure. $E_x$ and $E_y$

contributed somewhat to the field magnitude, but the contributions were small. The dominance of the vertical component of the field was found to be true in almost all of the penetrations even when a penetration of the anvil was made close to the convective core of the storm. Note that the sharp increase in electric field occurs more than 3 min (~20 km) after the aircraft entered the anvil and a minute (~7 km distance) before the aircraft passed over precipitation that was reaching the ground (Figure 2). The measurements shown in Figure 2 are typical of those from other penetrations, some of which were farther from the core and the
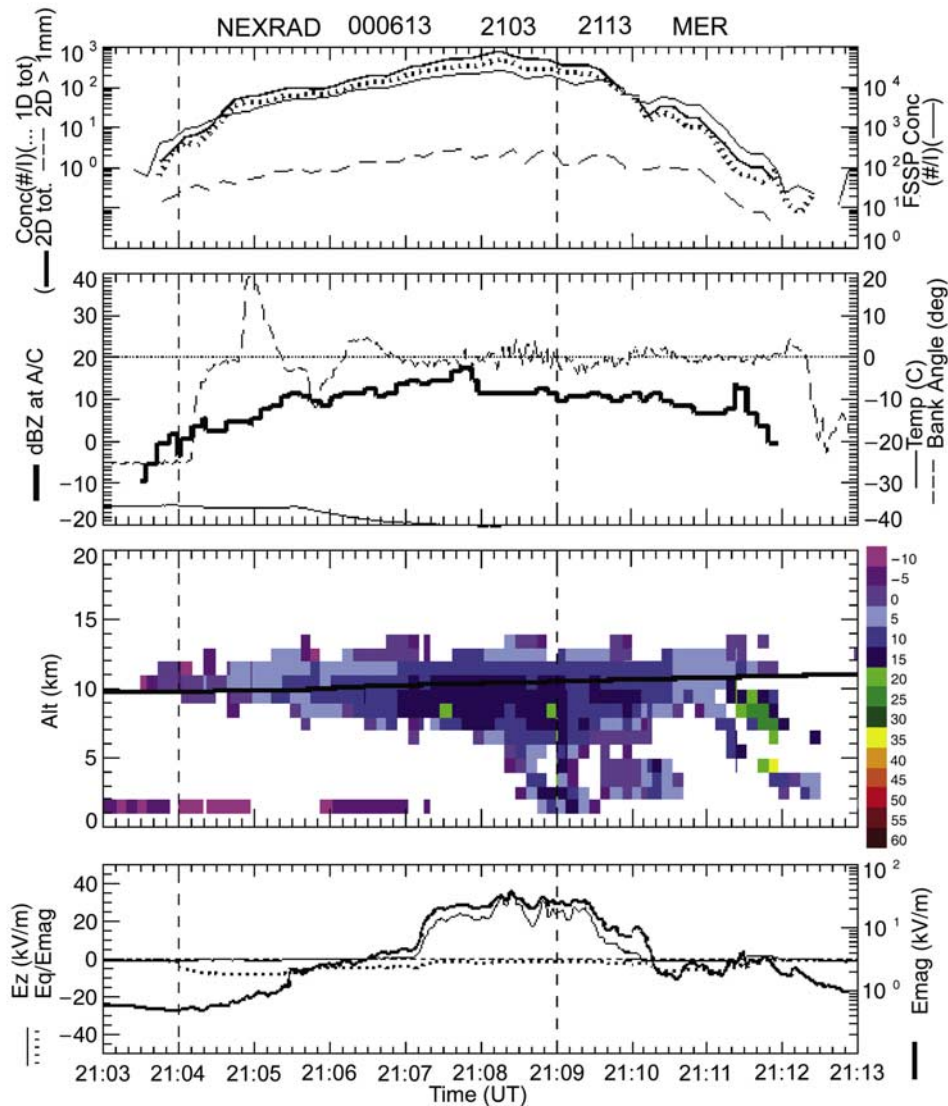
**Figure 2.** MER plot for 2103–2113 on 13 June 2000. Top panel: Particle concentrations from different instruments: FSSP total concentration = light, solid line; 2D-C total concentration = bold, solid line; 2D-C concentration >1 mm = dashed line; 1D-C total concentration = dotted line. Second panel: Reflectivity at the aircraft location, bank angle of the aircraft, and ambient temperature. Third panel: Curtain of radar reflectivity above and below the aircraft (the numbers to the right of the color scale show the upper limit of reflectivity for each color interval); bold line = aircraft altitude. Bottom panel: $E_z$, the vertical component of electric field, is a thin line and referenced to the linear scale on the left. $E_q/E_{mag}$, shown as a dotted line, is also referenced to the left scale ($E_q$ is the field due to the charge on the aircraft). $E_{mag}$, the scalar magnitude of the vector field, is shown as a bold line and referenced to the log scale on the right.

low-level convection seen on the west side of the storm in Figure 1.

[25] Even though this pass of the Citation was moderately close to the core of the storm (Figure 1) and the core was still producing lightning, the Rosemount Icing Detector showed no evidence of supercooled water being present. All passes were examined for evidence of the presence of any supercooled liquid water in these anvils, but none was found [*Schild*, 2003]. We have confidence in the ability of the Rosemount probe on the Citation to detect supercooled liquid water because it did show supercooled liquid water to be present in some convective cores. Although supercooled water was not present at the aircraft penetration altitudes of

8–11 km, the laboratory work of *Jayaratne et al.* [1983] has shown that a limited amount of charge transfer can occur between colliding ice particles, albeit very, very small. *Dye and Willett* [2007] argue that given the broad ice particle size distributions and the extended times available for particle collisions in long-lived anvils some charge transfer might be occurring, but at a much slower rate than occurs in convective cores.

[26] Particle concentrations in different size ranges are shown in Figure 3. Unlike the abrupt increase in electric field (Figure 2), the concentration of particles in different size ranges did not show abrupt changes but gradually varied as the Citation flew from the edge of the anvil
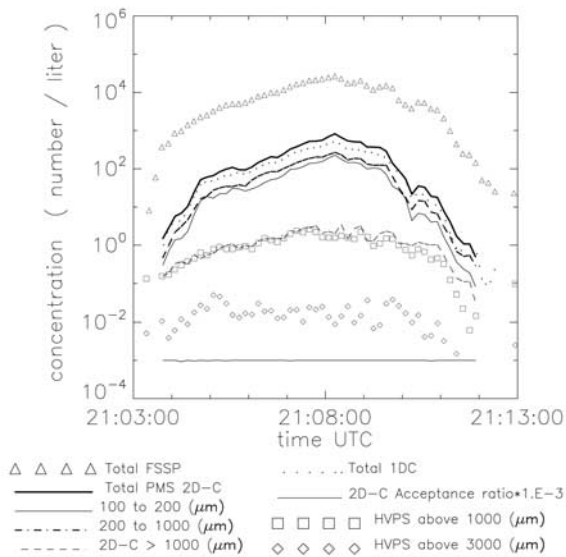
**Figure 3.** Time series plots of 10-s average values of particle number concentration for different probes and size ranges as indicated. The trace for the 2D-C >1000 $\mu$m is the dashed line almost on top of the squares for HVPS >1000 $\mu$m.

toward the more dense part of the anvil and then decreased more rapidly on the western side of the anvil. The relative increase in concentration was larger for the smaller particles (shown by the FSSP and the total concentration of the 1-DC and 2D-C probes) than for the larger particles (shown by particles >1 mm from the 2D-C and HVPS). The concentration of particles >3 mm (measured by the HVPS) changed near the anvil edge, but there was not a distinct trend during most of the penetration. Note that the concentrations of small- and intermediate-sized particles were greatly reduced near the anvil edges as would be expected as a result of evaporation and mixing.

[27] Figure 4 shows examples of images from the 2D-C for the pass of Figure 1. Images of the particles from CPI and 2D-C showed that smaller particles were primarily frozen cloud droplets. The intermediate-sized particles were usually irregularly shaped, but pristine crystals such as plates were occasionally seen. The particles larger than 500 $\mu$m were primarily aggregates or polycrystals [*Bailey and Hallett*, 2002]. Near convective cores some rimed particles were seen. A cursory examination of CPI particle images for some of the cross-anvil penetrations did not show a change in particle type associated with the abrupt increases of electric field, but this deserves a more careful study.

[28] Plots of the size distributions of particle number concentration and cross-sectional area at different locations across the anvil from near the edge to the dense part are presented in Figure 5. Because both size and concentration range over a few orders of magnitude, these distributions are plotted in the form $dn_i = fn(\log D_i) \, d(\log D_i)$, where $dn_i$ is the concentration of particles in the size interval $i$ and $D_i$ is the mean size of particles in that interval. $dD_i/D_i$ was substituted for $d(\log D_i)$ because the particles are accumulated in linear size intervals. Thus, $dn_i = fn(\log D_i) \, dD_i/D_i$. The units of $dn_i$ are $cm^{-3}$.

[29] The cross-sectional area for each particle was determined from 2D-C and HVPS images based upon the number of pixels occulted by the particle as it transited the laser beam of that probe. Particle areas were then accumulated in the same size bins as were the number concentrations. The particle size distribution plots in Figure 5 show the agreement between the different probes as well as more details of the distributions themselves. As previously noted in Figure 3, successive size distributions in Figure 5 show increases over the entire size range as time progressed, reaching a peak near 2108 when the Citation was flying in higher reflectivity.

[30] Excluding the FSSP measurements, the mode of the number concentration plots was at sizes of 50–300 $\mu$m, while the mode of cross-sectional area was at sizes of 200–2000 $\mu$m. *Willett and Dye* [2003] argue that the particle cross-sectional area is one of the primary factors controlling the rate of decay of electric field in the anvil. The cross-sectional particle area in different size ranges is plotted in Figure 6 for the measurements from the 2D-C and the HVPS. This figure shows that in the main body of the anvil, the area for sizes between 0.2 and 1 mm was almost one order of magnitude greater than the area for particles >1 mm in size. But near the edges of the anvil (near 2104 and 2011), the particles >1 mm contributed almost as much to the total area as the 0.2- to 1-mm particles.

[31] During this penetration across the anvil, the total particle cross-sectional area increased by more than an order of magnitude from the anvil edge to the dense part of the anvil. Consequently, the time expected for field decay is expected to increase by similar amounts. Calculations for this penetration presented by *Willett and Dye* [2003] of "E Time Scale," an estimated upper bound on the time required for the electric field magnitude to decrease from 50 to near 0 kV m[1] based on an observed particle size distribution, gave E Time Scale values of ~300 s (5 min) at the anvil edge but ~5700 s (93 min) in the dense part of the anvil near 2108. Thus, at the edge of anvils the electric field decay should be very rapid but the decay is expected to be much, much slower in the dense part of the anvil. Because sedimentation and turbulent mixing, leading to evaporation, are the main mechanisms acting to erode the particle size distribution, the rates of mixing and sedimentation may also be important factors in determining the electric field decay.

### 3.2.  24 June 2001

[32] On 24 June, widespread convection started at 1630 with a cold front approaching from the north. By 1800 storms covered central Florida with a line of strong convection oriented along the east coast moving over KSC and Cape Canaveral. One of these cells spawned a tornado that touched down in the Eastern Range at 1830. The Citation took off at 1803 and almost immediately climbed into an anvil that extended 40 km to the northeast of KSC. It then made several penetrations in the northeast and southwest directions moving away from and toward the line of convective cores, along and into the direction of the wind. The track of the aircraft toward the convection from 1849 to 1858 is shown overlaid on CAPPIs in Figure 7. The figure shows the anvil ahead of the line of convection and a trailing stratiform region behind the line, characteristics of
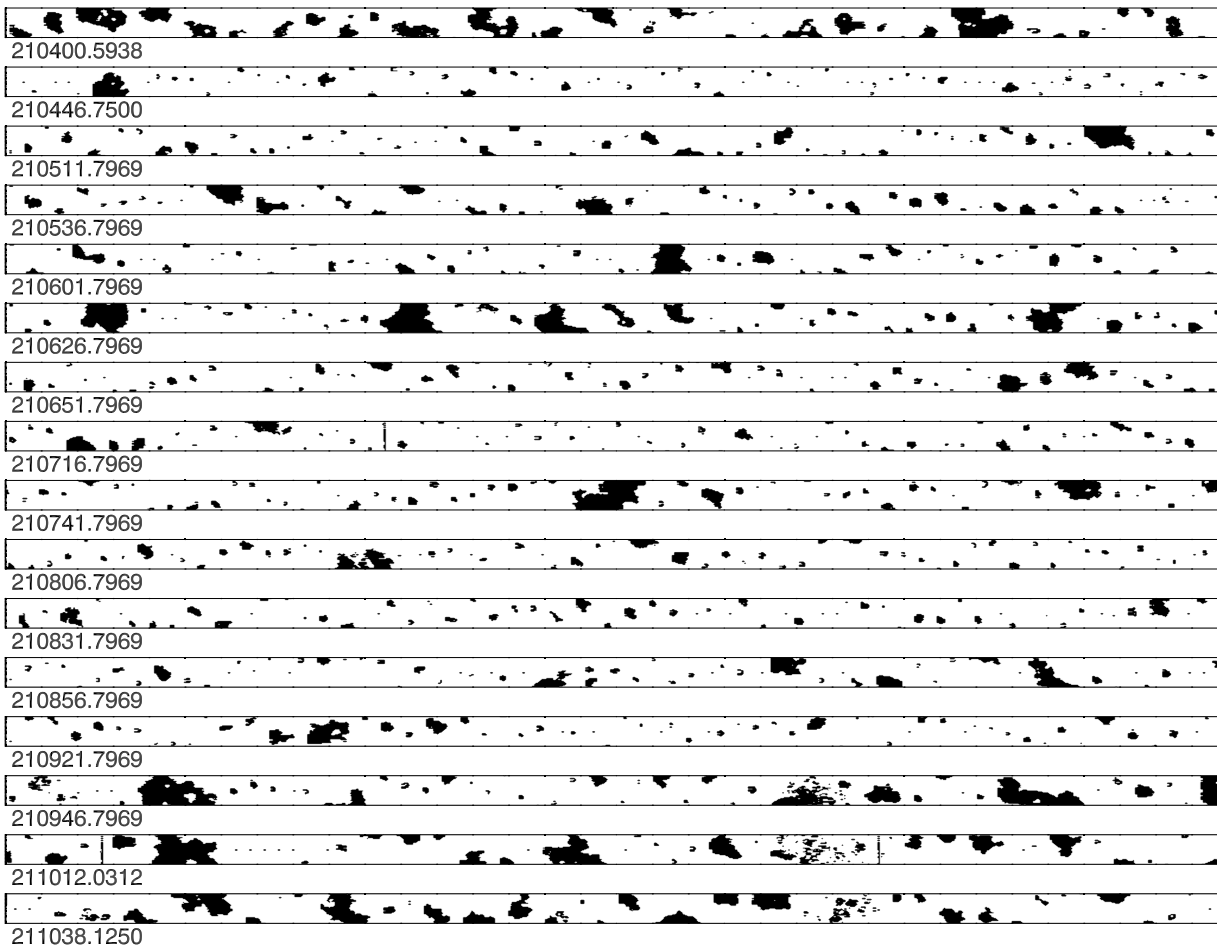
**Figure 4.** Buffers of particle images from the 2-DC probe. The vertical dimension of each row is ~1 mm. Text at the top of each buffer (row) shows the flight day (M/D/Y); the start time of the first image in that buffer; the time of the last image in the buffer; DeltaT = the elapsed time to fill the buffer; TAS = true airspeed of the aircraft. Only one out of every hundred buffers recorded is displayed.

mesoscale convective systems. The corresponding MER plot of particle concentration, reflectivity curtain along the aircraft track, and electric field measurements are presented in Figure 8.

[33] Figure 8 shows an example of the changes in electric field observed when penetrations were made from the downwind tip of the anvil toward the convective core along the anvil axis. Particle concentrations and reflectivity increased smoothly from the edge of the anvil inward but there was an abrupt, rapid increase in electric field (between 1852 and 1853) even in this intense storm, which was very actively producing lightning at the time of this penetration. As with the 13 June case of Figure 2, the field increase occurred near a reflectivity of 10–15 dBZ. The bottom panel of Figure 8 shows large variability and changes in polarity of $E_z$ during this constant altitude pass, indicating the complex charge structure of this anvil.

[34] Some of these field changes were probably produced by nearby lightning. The LDAR VHF sources (not shown) showed that lightning extended out almost as far as the western end of the Citation track at ~1858. The particle concentrations measured by the 2D-C on 24 June (Figure 8) are a little higher than the maximum total 2D-C concentration shown in Figure 2 for 13 June, but considering the

intensity of this storm were rather comparable. The electric field magnitude was also comparable for the two cases.

## 4. Synthesis of Measurements in Anvils

[35] In the previous section, we showed examples of the electric field, particle concentration, and radar reflectivity measurements for two separate anvils. In this and in the following sections, we examine the relationships between these parameters for all of the ABFM II measurements in anvils. To examine these relationships, we produced a data set for each Citation flight that included 10-s averages of measurements of standard state parameters such as ambient temperature, aircraft altitude, attitude, and position; the three components and magnitude of the electric field; and particle concentrations in different size categories for each of the particle probes. These airborne measurements were then merged with measurements of the reflectivity at the aircraft location and other spatial averages of reflectivity centered on the time and position of the aircraft. In this section, in order to reduce the statistical uncertainty in the particle concentration measurements and the point-to-point scatter in reflectivity values, we have used 30-s averages of aircraft measurements and 3-km cube averages of reflectivity.
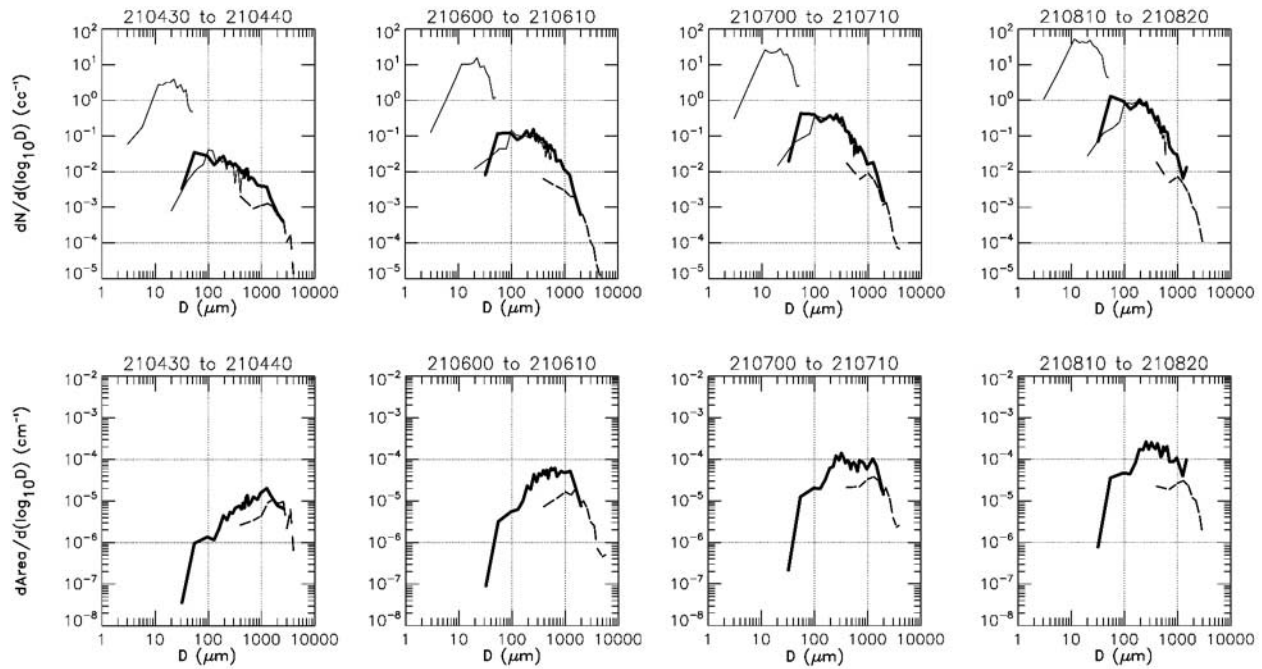
**Figure 5.** Top: Particle size distributions (10-s integration times) for the periods indicated during the Citation pass shown in Figures 1 and 2. Bottom: Particle cross-sectional area distributions from the 2D-C and HVPS for the same 10-s time periods. Light line on the left side of number plots = FSSP; bold line = 2D-C; dotted line near the 2D-C line = 1D-C; dashed line on right of each plot = HVPS.

At a flight speed of $100-120$ m s$^1$, 30 s corresponds to a distance of $3.0-3.6$ km.

[36] Although several different types of clouds were sampled by the aircraft during the ABFM II project, we present here only those measurements made in or near anvils. We defined an anvil as a cloud formed by transport away of material from the convective core(s) by upper level winds or divergence at the top of a convective core. To be considered an anvil, we further required that the cloud in question had a radar definable base without precipitation reaching the ground. This then excluded some measurements that were made during penetrations near convective cores where precipitation was reaching the ground or in precipitating stratiform regions. The total number of 30-s averages in this composite data set of anvil measurements was 2190 from 29 different anvils and 79 separate penetrations. Most of the aircraft penetrations were at altitudes of $8-10$ km.

### 4.1. Similarity of the Microphysical Properties of Dense Anvils

[37] The microphysical measurements in the dense part of the anvils, i.e., the regions with the highest reflectivity and greatest particle concentrations, showed a lot of similarity from flight to flight and anvil to anvil. This is in part because >65% of the measurements in anvils made during ABFM II were at altitudes of $8-9.3$ km. The similarity in the particle size distributions in the dense part of the anvils is shown in Figure 9 where the concentration of particles >1 mm measured by the 2D-C for each 30-s period is plotted versus the total concentration of particles measured by the 2D-C. The measurements were broken into two

groups, those with field magnitudes $\geq 10$ kV m$^1$ (black) and those with field magnitudes <10 kV m$^1$ (gray).

[38] Figure 9 shows that there is an almost linear relationship in this log$-$log plot in the dense part of the anvils where the field magnitude was >10 kV m$^1$. A linear least
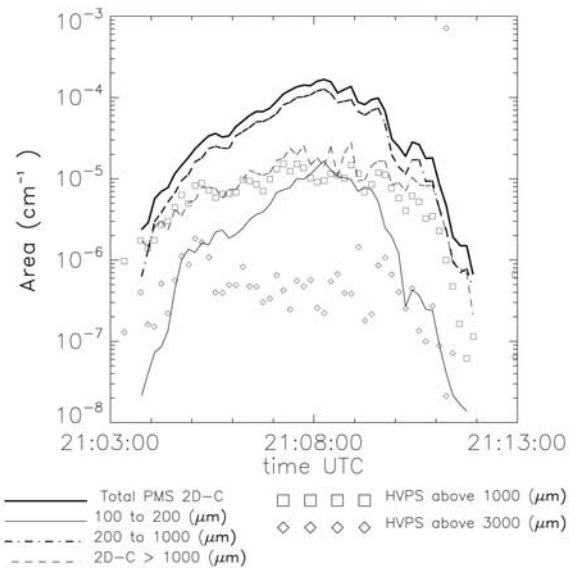


**Figure 6.** Time series plot of 10-s average values of particle cross-sectional area in different size intervals derived from 2D-C and HVPS measurements as indicated. The trace for the 2D-C >1000 $\mu$m is the dashed line almost on top of the squares for HVPS >1000 $\mu$m.
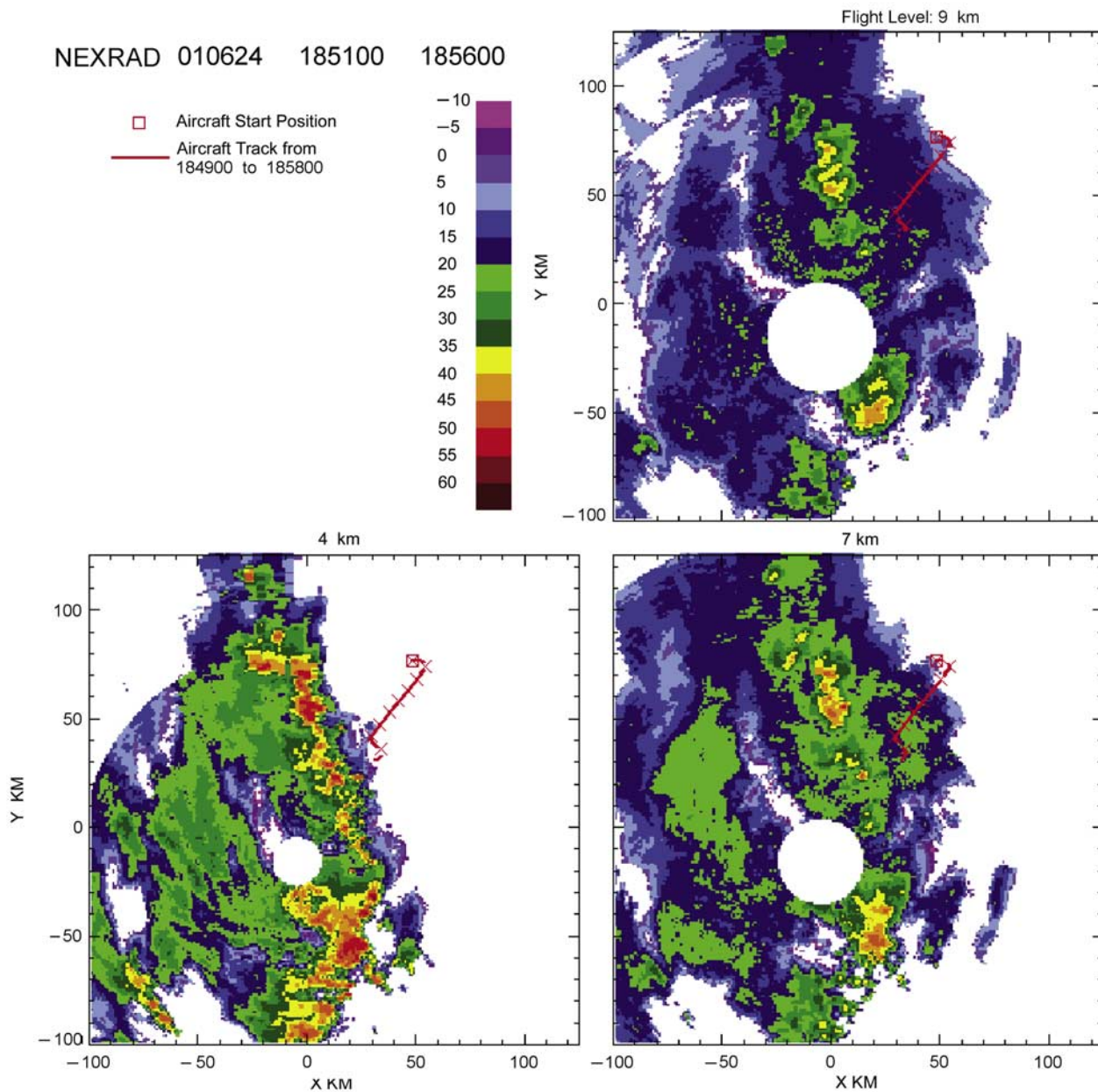
**Figure 7.** CAPPIs of reflectivity at 4, 7, and 9 km for 24 June 2001 from the NEXRAD 1851–1856 volume scan with aircraft track from 1849 to 1858 overlaid in red. The initial aircraft position is shown by a square with Xs plotted at each successive minute along the track.

squares fit to the logarithms of those points with field magnitude $\geq 10$ kV m[1] (the 456 black points) had a correlation coefficient of 0.69, which has high statistical significance. This best fit line shows almost two orders of magnitude increase of the total 2D-C concentration for each order of magnitude increase in the concentration of particles greater than 1 mm. This result is similar to that shown in Figure 3 for only one penetration, that is, as the aircraft flew from the edge of the anvil toward the dense part of the anvil the concentration of small- and intermediate-sized particles increased more than the concentration of the larger particles.

[39] Although there is scatter, the variation of particle concentration from case to case was within a factor of 2–3

in the dense anvils. In the edges of the anvil where concentrations are smaller, there was much more variation. The majority of the points with high concentrations of both small and large particles were the same regions with fields magnitude >10 kV m[1]. Contrastingly those regions with lower particle concentrations corresponding to edges or other less dense parts of the anvil were almost devoid of points with field >10 kV m[1].

[40] Both aggregation and sedimentation should alter the particle size distribution in an anvil, and we have some evidence of this in the measurements made during spiral descents. On 24 June 2001, a descent was made from 9.2 to 4.7 km ($-31$ to $-4°$C) from 1947 to 2001 in a region that
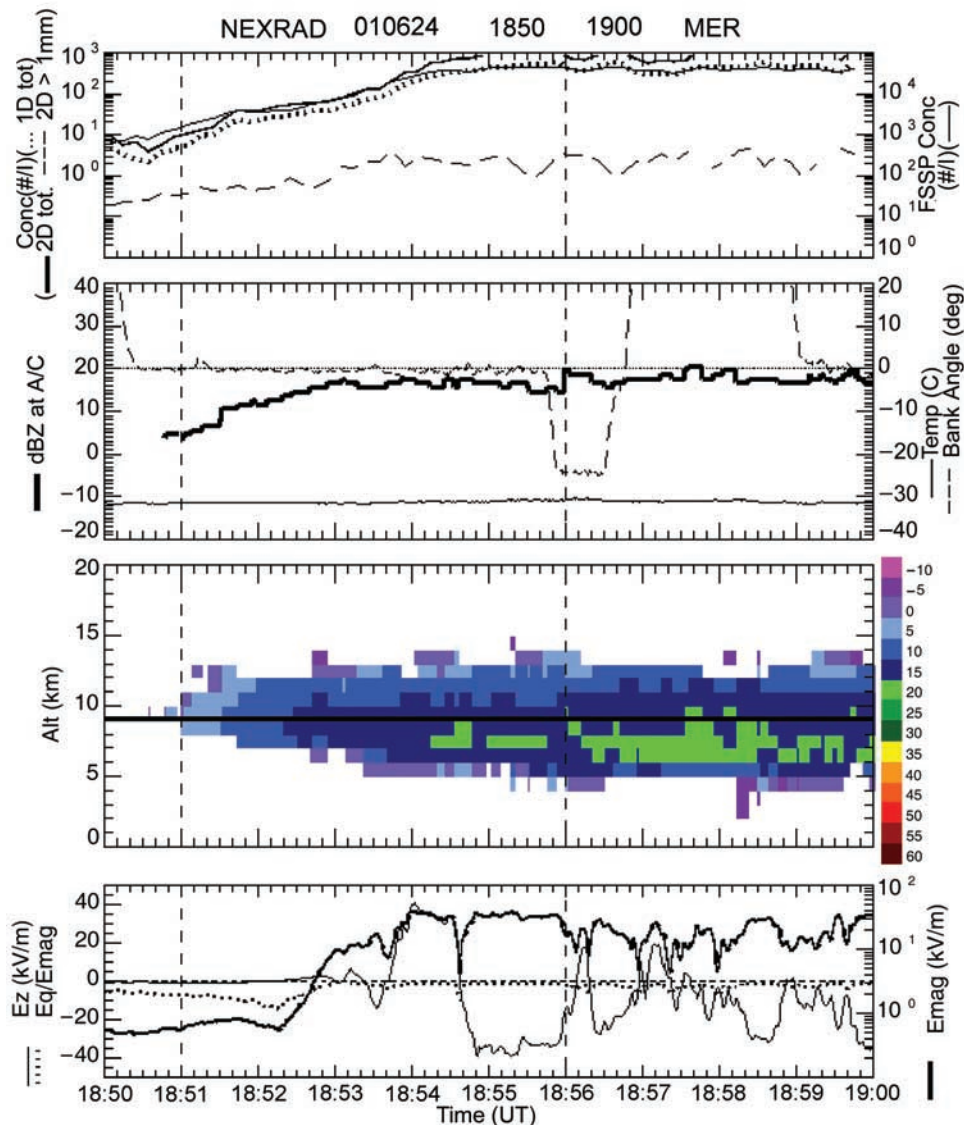
**Figure 8.** Same as Figure 2 except 1850–1900 on 24 June 2001.

was the transition zone between the anvil and a broad mid-level stratiform region with 20–25 dBZ reflectivity at 6–8 km altitude, but without precipitation reaching the ground. The electric field magnitude was 10–30 kV m[1] for much of the descent. The concentration of the small- and intermediate-sized particles decreased by a factor of 3–4 and the concentration of the particles >3 mm increased by a factor of about 5, thus showing the effects of sedimentation and aggregation. The concentration of particles >1 mm increased less than a factor of 2. In the altitude interval of 9.2–8 km, where >65% of the ABFM II anvil penetrations were made, the decrease in small- to mid-sized particles was small and the increase in >3 mm particles was less than a factor of 2.

## 4.2. Relationship Between Radar Reflectivity and Particle Concentration

[41] Figure 10 shows the average reflectivity in a 3-km cube centered on the aircraft altitude and location plotted as a function of particle concentration for different size ranges. The reflectivity of the 1-km grid pixels was averaged in dBZ. Pixels with no detectable reflectivity were not included in the average, and to be included in the data set, we required that at least 16 of the 27 one-kilometer pixels in the 3-km cube contain detectable reflectivity. Three kilometers was chosen as it approximately corresponded to the distance flown by the aircraft in 30 s. In addition, the 3-km cube average smoothed some of the pixel to pixel variation of the 1-km gridded radar measurements and also helped to compensate for the scan gaps in radar coverage when the radar elevation sweeps did not overlap.

[42] Although there is a lot of scatter in these plots, particularly for the 100- to 200-$\mu$m and 200- to 1000-$\mu$m particle size ranges, all plots showed a trend of increases in reflectivity with increases in concentration in all size ranges. Linear least squares fits to the reflectivity in dBZ versus the logarithm of particle concentration gave correlation coeffi-
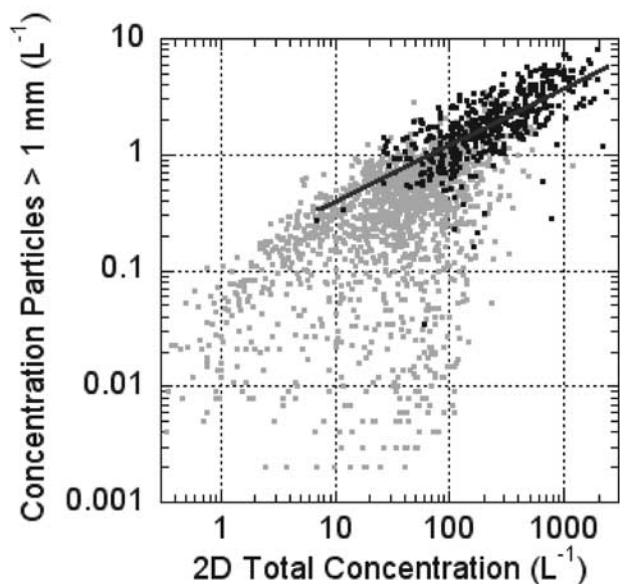
**Figure 9.** Scatterplot of 30-s averages of total particle concentration measured by the 2D-C versus the concentration of particles >1 mm measured by the 2D-C. The points with field magnitude $\geq 10$ kV m[1] are plotted in black while those with field <10 kV m[1] are gray. There are a total 1998 points in this plot of which 456 points had field magnitudes $\geq 10$ kV m[1]. The straight line is a least squares fit to only those points with $E \geq 10$ kV m[1].

cients of 0.50, 0.58, 0.68, and 0.58 for plots C, D, E, and F, respectively. Although the correlation coefficient of plot F (for the concentration of particles >3 mm) is less than that for plot E (for the concentration of particles >1 mm), visually there appears to be less scatter in plot F for points with the greatest particle concentration. Because the radar reflectivity is proportional to the sixth power of particle size, we expect the reflectivity to be dominated by the concentration of the largest particles, as suggested in Figure 10. The ABFM II observations in these Florida anvils do not show unusual behavior in the relationship between particle concentration and reflectivity. Figure 10 is shown here primarily to help interpret the results of the next two sections, where the electric field magnitude is shown not to have a well-behaved relationship to either particle concentration or radar reflectivity.

### 4.3. Relationship Between Electric Field and Particle Concentration

[43] The relationship between electric field and particle concentration is shown in Figure 11. Unlike the trend of increasing reflectivity with increasing particle concentration shown in Figure 10, both the total 2D-C concentration and the concentration of particles >1 mm shown in Figure 11 exhibit a clear change in character at $1-2$ kV m[1]. For electric fields >2 kV m[1], there was a gradual but not pronounced increase in the particle concentrations as electric field increased from 2 to >30 kV m[1]. But for electric fields <2 kV m[1], there is a "knee" and much more variation in the particle concentration. This knee is a result of the rather abrupt transition in electric field noted previously and shown in Figures 2 and 8. The plots show a threshold

behavior with only a few points in the lower right part of the plots. The points in Figure 11 are distributed throughout the anvil cases. Thus the knee in these plots was not from any specific case but was a feature that is representative of all the ABFM II anvil measurements. This change in behavior suggests a change in physical processes or perhaps in the balance between different physical processes. We will explore some possible explanations for this change in behavior in Section 6 below.

### 4.4. Relationship Between Electric Field and Reflectivity

[44] The relationship between the electric field magnitude and the 3-km cube average reflectivity is presented in Figure 12. Like the plots of particle concentration versus field magnitude shown in Figure 11, these plots show a change of character or knee at $1-2$ kV m[1]. This is not too surprising in view of the monotonic trends shown in Figure 10 above. For electric fields less than 2 kV m[1], the average reflectivity spanned a range from 10 to >20 dBZ with many points having a field <3 kV m[1] but a reflectivity of $10-20$ dBZ, showing that higher reflectivity is not necessarily a good predictor of strong electric fields. However, only a few points with electric field >3 kV m[1] have a reflectivity less than 5 dBZ. There is a reflectivity threshold below which thunderstorm strength electric fields (>~5 kV m[1]) were not found in ABFM II anvils.

### 5. Exploring Possible Radar Parameters for Use in an LLCC

[45] The results shown in Figure 12 gave promise that a radar-based reflectivity parameter might be a useful diagnostic for determining the possibility of high electric fields in anvils and for developing improved Lightning Launch Commit Criteria (LLCC) for anvils. However, since there were a few points in the lower right quadrant of Figure 12 that had electric fields >3 kV m[1] with average reflectivity less than 5 dBZ, we explored other possible spatial averages of reflectivity.

[46] Before examining other radar parameters, we wanted to know the maximum electric field that might present a threat for triggering lightning in these anvils. This is a topic of current research and a detailed discussion is beyond the scope of this paper. Extrapolation of the rocket triggered lightning studies of *Willett et al.* [1999] to anvil altitudes suggested that electric fields <3 kV m[1] are not capable of triggering lightning to large vehicles like the Space Shuttle and the Titan booster at anvil altitudes. This is the value currently used by the Air Force and NASA in the existing LLCC. By way of comparison, during ABFM II in dense parts of anvils field magnitudes of $30-60$ kV m[1] were frequently observed during penetrations near the convective cores of storms and $10-30$ kV m[1] in anvils tens of kilometers downwind of the core. Fields of $100-150$ kV m[1] have often been observed in mature thunderstorms [*MacGorman and Rust*, 1998, pp. $174-177$].

[47] Figure 13 shows the relationships between electric field and four different spatial averages of reflectivity. In these plots, we have used 10-s averages of electric field and we have filtered the entire anvil data set to remove points for which the aircraft was within 20 km of a convective core
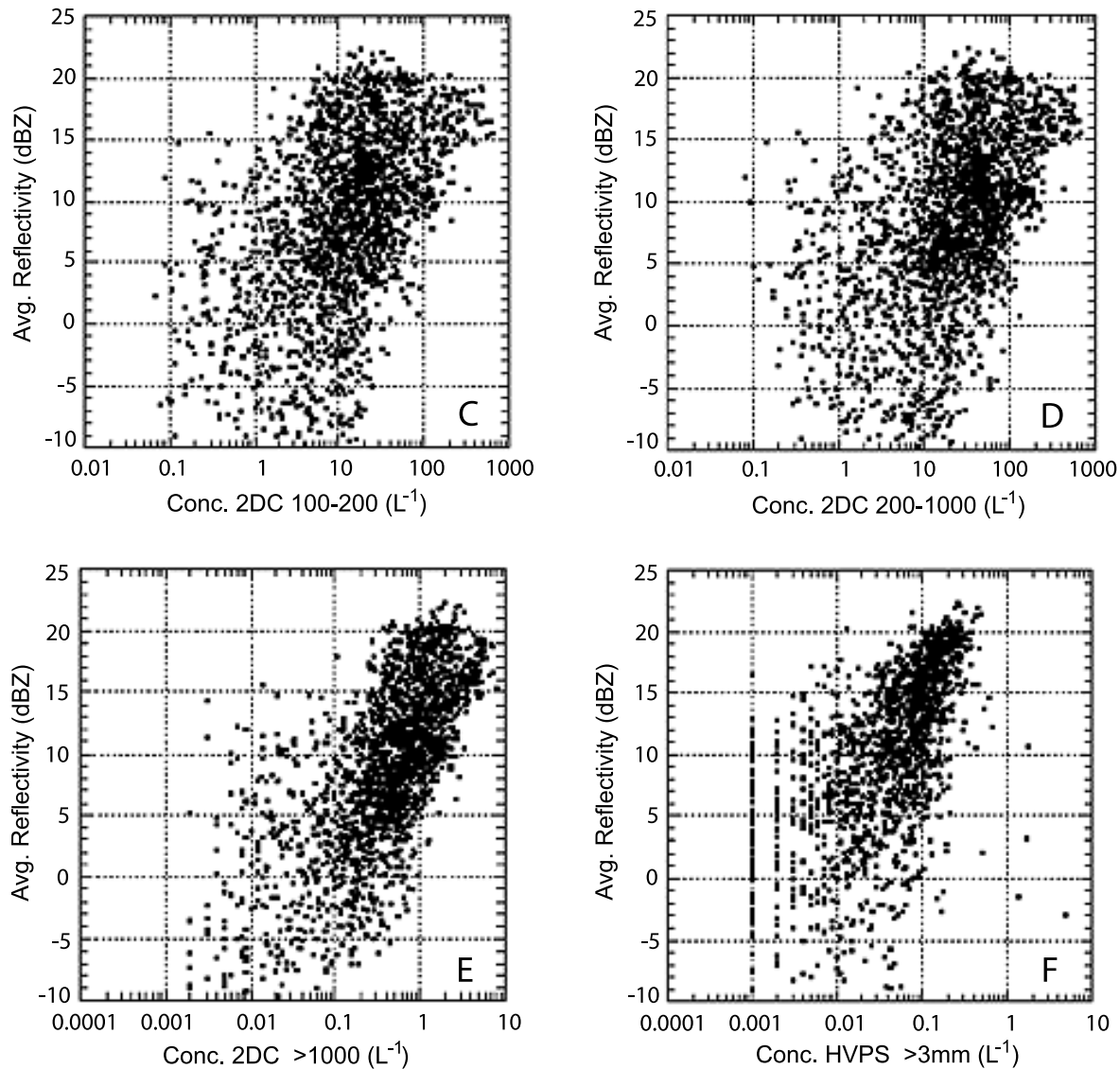
**Figure 10.** Scatterplots of particle concentrations in different size categories (100–200 μm; 200–1000 μm; 2D-C ≥1 mm; and HVPS ≥3 mm) versus the average reflectivity within a 3-km cube centered on the altitude and position of the aircraft. There were about 2000 points in Figures 10a, 10d, and 10e, and 1500 in Figure 10f.

with reflectivity >35 dBZ at 4 km altitude or greater in order to avoid regions of rapid field intensification associated with the cores. We also have removed points for which the aircraft was within 20 km of any lightning detected by either LDAR or the CGLSS within the previous 5 min in order to avoid regions directly influenced by recent lightning. Additionally, we limited these averages of reflectivity to altitudes ≥5 km, roughly the freezing level in Florida during the summer. The plot on the lower right shows results for the 3-km cube reflectivity average and is similar to Figure 12, except for the core and lightning filters mentioned above and except for the 10-s averages of electric field rather than the 30-s averages used previously. The results are similar to those of Figure 12 with a few points that have $E$ >3 kV m$^1$ and reflectivity <5 dBZ.

[48] A reflectivity parameter averaged over a volume larger than 1- or 3-km cube has the possibility of including regions of high reflectivity that might contain substantial charge near, but not at the aircraft position. It has the additional advantage that averaging over a larger volume will compensate for any unsampled scan gaps and radar propagation effects. The upper left plot labeled AVG 11 × 11 reflectivity on the ordinate shows the average dBZ reflectivity calculated from 5 km altitude (approximately the 0C level) to the top of the cloud over an 11 × 11 km area extending horizontally 5 km in the north, south, east, and west directions from the 1-km grid point containing the aircraft position. The lower left plot labeled AVG 21 × 21 reflectivity on the ordinate is similar except that the volume average is calculated over an area extending 10 km in each
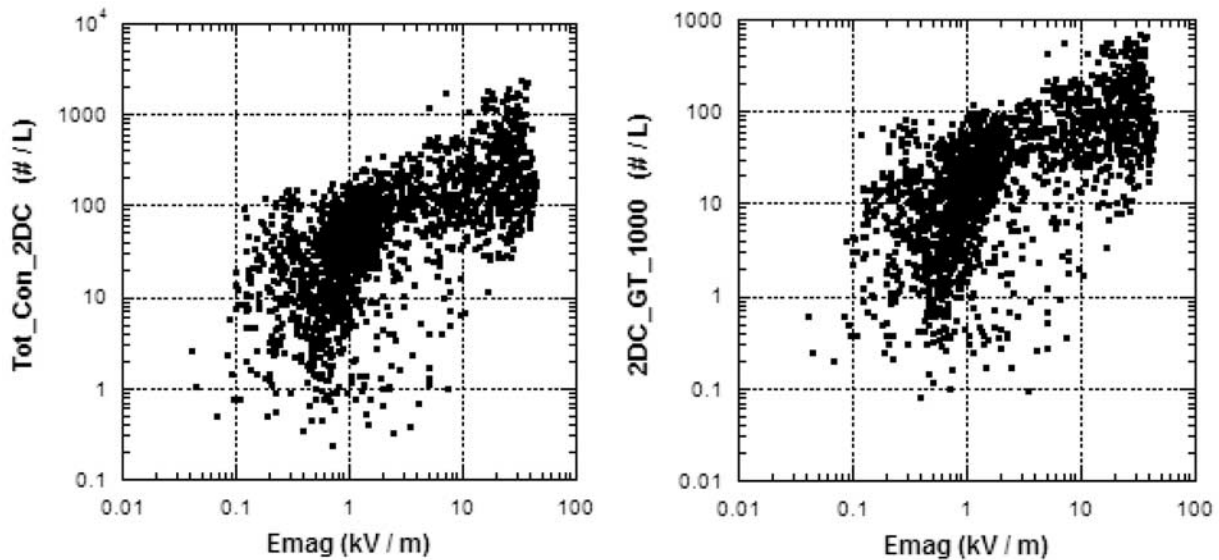
**Figure 11.** Scatterplot of electric field versus total particle concentration measured by the 2D-C (left) and concentration of particles >1 mm size (right) for the ABFM II anvil data set. Each figure contains about 2100 separate 30-s averages. Note that the concentration scale is different in the two plots.

direction from the aircraft position. These two plots show very similar results.

[49] A shortcoming of the volume averages is that averaging the reflectivity within a box or column ignores potentially important information on the depth of the anvil. A thin anvil might have the same average reflectivity as a much deeper anvil, but deeper anvils are more likely to contain charge. The upper right plot of Figure 13 shows the $11 \times 11$ Volume Averaged Height Integrated Radar Reflectivity (VAHIRR) [*Bateman et al.*, 2005]. This parameter was calculated by multiplying the $11 \times 11$ reflectivity averaged in dBZ by the average radar thickness of the anvil in km over the $11 \times 11$ km area. Unlike the $11 \times 11$ average reflectivity plot, in the upper right quadrant the $11 \times 11$ VAHIRR plot shows high values of reflectivity with high values of field magnitude. It has only one point in the lower right quadrant for VAHIRR <25 dBZ km and electric field >3 kV m[1]. A statistical analysis of extreme values [*Reiss and Thomas*, 2001] by Dr. Harry C. Koons (personal communication) for the $11 \times 11$ km VAHIRR ≤10 dBZ km (equivalent to an average of 10 dBZ in a 1-km-thick anvil or 2 dBZ in a 5-km-thick anvil) showed that the probability of having an electric field >3 kV m[1] was less than 1 in 10,000. VAHIRR is now being used by the Air Force and NASA in new Lightning Launch Commit Criteria for anvils.

## 6. Discussion

[50] In previous sections, we have shown that along a penetration the electric field increased abruptly in contrast to the more smoothly changing particle concentrations or reflectivity. This behavior was apparent for individual penetrations as well as in a statistical sense for all of the anvil measurements. In this section we explore possible causes for this behavior.

### 6.1. Screening Layers

[51] At cloud boundaries the electrical conductivity changes significantly. If there is a component of electric field normal to the cloud boundary fast ions can attach to cloud particles to produce charge layers that tend to "screen" the outside air from elevated fields in the lower conductivity interior of the cloud [e.g., *Klett*, 1972], hence the name screening layer. *Vonnegut et al.* [1966] and *Blakeslee et al.* [1989] have measured strong electric fields above the top of convective regions of thunderstorms and have concluded that screening layers were not present in the
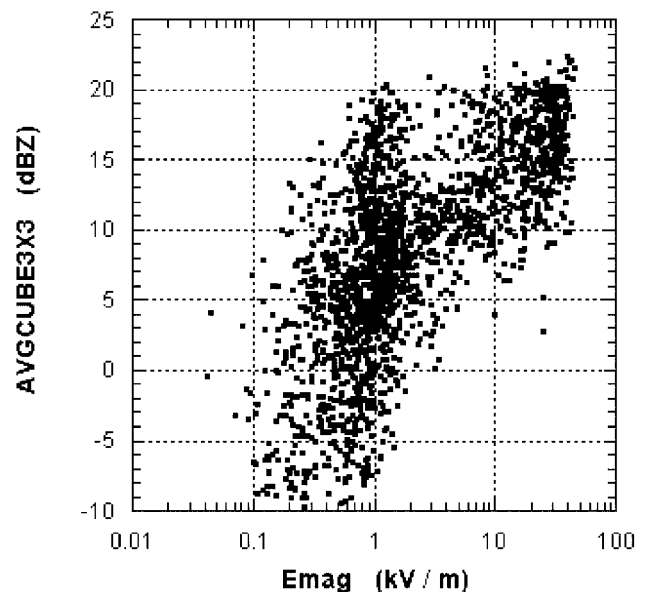


**Figure 12.** Scatterplot of electric field magnitude versus $3 \times 3 \times 3$ km cube average reflectivity for the ABFM II anvil data set.
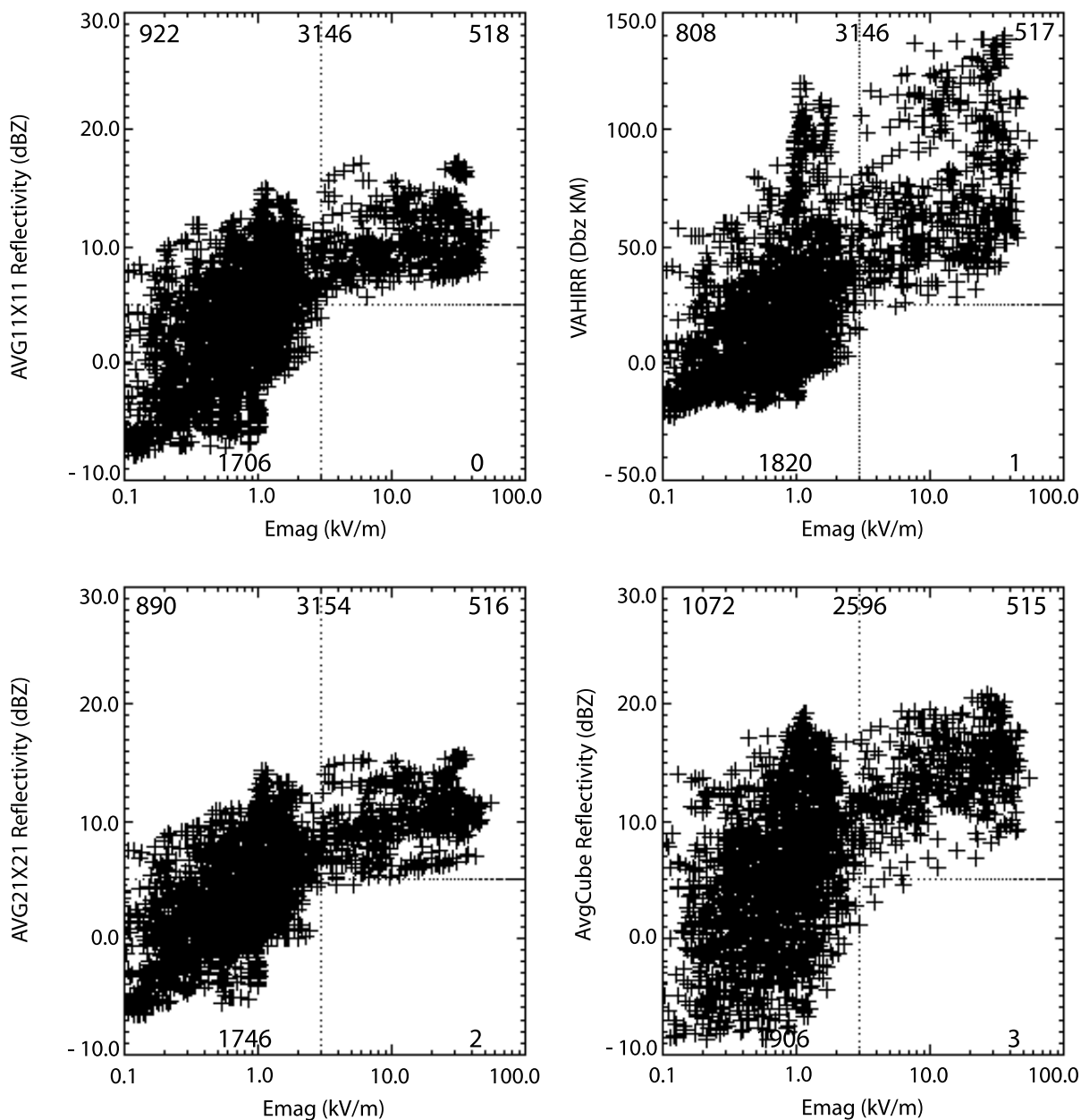
**Figure 13.** Electric field magnitude ($E_{mag}$) versus reflectivity for four different spatial averages of reflectivity (see text.) The number in the top center of each plot gives the total points in that plot with the numbers near the corners of each plot showing the number of data points in each quadrant of that plot.

convective turrets because of rapid mixing and entrainment near the cloud boundaries. At the top and bottom of stratified anvil clouds that contain net charge, however, balloon-borne measurements have found screening layers a few hundred meters thick [e.g., *Winn et al.*, 1978; *Marshall et al.*, 1984; *Byrne et al.*, 1989]. In principal, such layers might build up around the entire periphery of an electrified anvil, that is, on the vertical edges as well as on the top and bottom.

[52] There are two cases that concern us here. First, our observations of abrupt increases in field magnitude when flying horizontally into anvils might be due to vertical screening layers on the edges of these clouds. Such a vertically oriented charge layer near a cloud boundary could only be caused by a significant horizontal component of the field from net charge in the interior. If it existed, this layer of charge would produce a change in the horizontal field component perpendicular to the cloud edge as the aircraft penetrated the cloud.

[53] There are several reasons to doubt this explanation of our observations. We are not aware of any other measurements in the literature that document screening layers on the vertical edges of anvils. Our ABFM II measurements of the three components of electric field clearly show that the vertical component of the field, $E_z$, is almost always dominant and usually a factor of $3-10$ times or more as

great as the $E_x$ or $E_y$ component. Because the Citation penetrations were approximately perpendicular to the edge of the anvil, we should be able to detect the presence of a vertical screening layer as an abrupt increase in the magnitude of $E_x$ on entering or exiting the anvil, but we do not. Furthermore, the abrupt change in field magnitude was often observed at large distances from the edge of the anvil. For example, at 2107 in Figure 2 the abrupt field increase (primarily due to the vertical component) occurred more than 3 min ($\sim$22 km) after the aircraft entered the anvil. It is hard to imagine that turbulent mixing from the cloud edge would transport screening-layer charge this far from the edge of the anvil and still maintain the sharp gradient in field. Similarly, for 24 July the abrupt increase was >2 1/2 min ($\sim$16 km) from the downwind anvil tip detected by the particle probes. An examination of aircraft entrance and exit penetrations of anvils shows that for ABFM II anvils the average distance inside the anvil boundary at which the field magnitude exceeded 3 kV m[1] was about 3 km *Merceret et al.* [2007].

[54] The second case that concerns us here involves the horizontal screening layers that are known to occur on the top and bottom boundaries of electrified anvils. During a horizontal pass through such an anvil, the aircraft might dip into or out of a charge layer that was not perfectly flat as a result of gravity waves or other dynamics within the cloud. If the screening layer was sufficiently thin, this might result in the kind of abrupt increases and decreases in field magnitude (dominated by the vertical component of the field) that we observed, for example, in Figure 2.

[55] We also doubt this as an explanation of the abrupt field increases that we observed. In most cases when these events occurred, the Citation was flying well below (above) the top (bottom) of the anvil. For example, in Figure 2 at 2107 the abrupt field change occurred where the anvil thickness was 6–7 km and the aircraft was at least 2 km below the cloud top. Again, it is hard to imagine that turbulent mixing would transport screening layer charge this far from the top of the anvil and still maintain the sharp gradient. Turbulent mixing would act to smear out charge and smooth out the gradient of electric field. Similarly, for 24 July the abrupt increase was approximately in the vertical center of a 7-km-thick anvil. In summary, it does not seem possible that screening layers could explain an appreciable fraction of the sudden increases (and decreases) in field magnitude that were observed during ABFM II.

## 6.2. Charge Transport From the Storm Core

[56] Charge separation via the noninductive mechanism is thought to occur primarily in moderate updrafts or updraft/downdraft transition zones because that is the region in which supercooled liquid water, graupel, and numerous smaller ice particles coexist [e.g., *Dye et al.*, 1986]. Since moderate updrafts and updraft/downdraft transition zones occupy only a fraction of the horizontal area of the core of a storm, it seems reasonable to expect that strong electric fields would not be present across the entire breadth of the anvil, even near the convective core. The ABFM II measurements made near or only slightly downwind of a storm core (such as seen in Figure 2 for the 13 June case) indeed showed that strong fields did not exist across the entire anvil.

[57] If the abrupt changes in electric field occurred only during the cross anvil penetrations, the limited extent of charge transport could explain the behavior of our electric field versus particle concentration plots. However, Figure 8 for 24 June 2001 clearly showed an abrupt increase in electric field even when the aircraft flew along the main axis of the anvil toward the core of the storm. The updraft cells in multicellular storms, such as those investigated in ABFM II, often have lifetimes of 15–30 min and are episodic in nature, with new updrafts forming and intensifying while others are decaying. Evidence of this was clearly seen in the evolution of the reflectivity structure of ABFM II storms. Consequently, the time periods of charge separation and outflow of charged particles into the anvil should also be episodic. One would therefore expect that the charge distribution in the anvil would be granular with some regions containing more charge (stronger electric fields) than others. We see evidence of this in ABFM II measurements. As a parcel containing charge moves downwind in the anvil, turbulent mixing and electric field decay (see below) occur. These processes should reduce the gradient of electric field as well as the magnitude and thus the abruptness of electric field changes. Both the limited fraction of the storm core from which charged particles are advected, and the episodic nature of the updrafts is likely to play a role in explaining some of the abrupt changes in field that we observe.

## 6.3. The Rate of Decay of Electric Field by Conduction

[58] In a passive anvil, i.e., an anvil in which active charge separation is not occurring, the electric field should decay as the charge moves downwind of the convective core. *Willett and Dye* [2003] describe a simple model to estimate an upper limit to the decay time of electric field in a passive anvil in which there is a constant influx of cosmic rays, no turbulent mixing, no condensation, no evaporation or sedimentation of particles, and the absence of active charge separation. The mechanism for field decay in the model is the bulk conduction current inside the anvil that reduces the net charge contained in its interior. A modification of this simple model was used to estimate an upper limit to the decay time of electric field that would be expected for the along-axis anvil penetration shown in Figure 8. This case is particularly amenable to model analysis because the aircraft penetration from 1850 to 1856 was oriented upwind, from the tip of the anvil toward the convective core. Assuming that the anvil structure remained approximately steady state (which radar observations show to be valid), both electric field and particle concentration would decay while moving from the core to the anvil edge but remain essentially constant at each location along the aircraft track. In the calculations, the actually observed particle size distributions were used for the calculation.

[59] The results from the model gave a decay of electric field from 37.5 to 12 kV m[1] over a distance of 28 km compared to an observed decay from 37.5 to <1 kV m[1] in $\sim$10 km. Additionally the decay in the model was continuous and not nearly as rapid as the observed decay and sharp decrease in field seen between 1852 and 1853 in Figure 8. We conclude that decay of electric field due to conduction currents is inadequate alone to account for the

abrupt changes in electric field that we observed in this or other cases.

## 6.4. Enhancement of Electric Field in Long-Lived Anvils

[60] In a separate paper, *Dye and Willett* [2007] document that two of the long-lived ABFM II anvils developed horizontally extensive regions in which the electric field, the reflectivity, and the particle concentrations became very uniform and maintained strength over tens of minutes and tens of kilometers. They argued that charge separation occurring in the melting layer might be partially responsible for the prolongation of electric field in the long-lived anvils. However, because of the long time for ice particle interactions and the broad particle spectrum, charge separation might also have taken place at higher altitudes than the melting zone from either a noninductive or perhaps even an inductive charge separation mechanism involving ice particle collisions. Although the noninductive mechanism has been found to be most efficient when supercooled water is present, the work of *Jayaratne et al.* [1983] and others do show some charge separation can occur, albeit very much smaller, even in the absence of supercooled liquid water.

[61] *Dye and Willett* [2007] also inferred that a weak updraft must have been present in the two long-lived anvils. Unfortunately the wind measurements from the Citation were not reliable and often unusable, primarily because of the mass of ice particles ingested into the Pitot tubes.

[62] The strong fields observed in the enhanced portion of the anvils seemed to be associated with horizontally extensive (many 10 s of km) regions of 20–25 dBZ at 7 km. If the enhancement occurred in specific locations and not across the entire anvil, it is possible that the weak fields outside the enhanced regions would reflect the values expected from field decay in a passive anvil. However, when the aircraft entered the enhanced parts of the anvils there might be an abrupt increase in field along the track. This enhancement, if localized, could perhaps explain the abrupt increases in field for the aircraft penetrations in enhanced anvils such as 13 June 2000 and 4 June 2001. On the other hand, because the particle size distributions were observed to change slowly and smoothly, one would think that spatial changes in the resulting ice particle collision rates would also occur slowly and not lead to abrupt spatial changes in the charge structure and hence electric field.

## 7. Concluding Remarks

[63] This paper describes the ABFM II project that investigated electric fields, microphysics, and reflectivity in anvils, debris clouds, and regions with stratiform precipitation. It has focused on the anvil measurements and presents examples for two cases to illustrate the type of measurements made during ABFM II. The observations have shown that electric fields in anvils often increased from weak to strong much more abruptly than particle concentrations and reflectivity.

[64] In Section 6, we explored several reasons for the abrupt behavior of the electric field in relationship to particle concentration, and hence reflectivity. We suggested that the abrupt behavior in field observed for most of the cross anvil penetrations in passive anvils might be the result of the limited area of the storm core from which charged particles were being advected into the anvil. Additionally, the episodic nature of the updraft and hence charge advection from the core may explain some of the along-axis anvil observations. In long-lived anvils in which charge separation and subsequent development had occurred, the abrupt increases in electric field might be due to localized regions of charge separation, but this seems at odds with the smoothly varying particle concentration. The rapid rate of decay of electric field near the anvil edge due to conduction currents probably also made a contribution but on its own seems unlikely to explain the abrupt nature of the observed field increases in the interior of the anvil. Screening layers on the side of the anvil are unlikely to explain our observations. The abrupt nature of the observed electric field change needs further investigation with modeling studies that include explicit turbulence and mixing and detailed microphysical observations as well as additional observations.

[65] The composite measurements from all anvils investigated in ABFM II showed that when the average reflectivity, such as in a 3-km cube, was less than about 5 dBZ, the electric field magnitude was <3 kV m$^1$, a value that is highly unlikely to trigger lightning by the Space Shuttle or a similar launch vehicle. Based on this finding, we developed the Volume Averaged Height Integrated Radar Reflectivity (VAHIRR) which combines radar-based observations of a volume average reflectivity and the thickness of the anvil. VAHIRR is now being used to increase launch availability in new Lightning Launch Commit Criteria for anvils.

[66] The ABFM II measurements showed that the charge structure in these anvils is very complicated with the vertical component of the field often changing polarity during a single aircraft penetration across the anvil. Our ability to investigate and to understand the charge structure was inhibited because we were rarely able to make spiral descents or ascents due to restrictions by Air Traffic Control from the heavy air traffic in Florida. Additional field campaigns in a location in which vertical soundings can be made would be highly desirable.

[67] The extensive and detailed measurements of cloud particle concentrations, types, and sizes, electric field, and coordinated reflectivity obtained during ABFM II provide an excellent data set with which to investigate a number of physical processes in anvils, debris clouds, and stratiform regions of Florida thunderstorms. Possible topics include the charge separation mechanisms and related particle interactions apparently occurring near the melting zone and at higher altitudes in long-lived anvils; the changes in particle type (especially riming) during penetrations across an anvil; the examination of the charge structure in anvils; the evolution of the particle size distribution by aggregation and sedimentation in both high and weak electric field situations; and the kinematic mechanisms responsible for the updraft and hence enhancement of reflectivity in long-lived anvils. We hope that other investigators might pursue these and/or other topics using the ABFM II data set. Interested investigators may contact Frank Merceret at the Kennedy Space Center Weather Office (francis.j.merceret@nasa.gov) for access to the data.

## References

Bailey, M., and J. Hallett (2002), Nucleation effects on the habit of vapour grown ice crystals from 18°C to 42°C, *Q. J. R. Meteorol. Soc.*, 128, 1461–1484.

Bateman, M. G., et al. (2005), Comparison of in-situ electric field and radar derived parameters for stratiform clouds in Central Florida, paper No. P1.10 presented at the Conf. on Meteorol. Apps. of Lightning Data, AMS Annual Meeting, San Diego, Calif., 23–28 Jan.

Bateman, M. G., M. F. Stewart, R. J. Blakeslee, S. J. Podgorny, H. J. Christian, D. M. Mach, J. C. Bailey, D. Daskar, and A. K. Blair (2006), A low noise, computer-controlled, internally digitizing rotating-vane electric field mill for airborne platforms, *J. Atmos. Ocean. Technol.*

Blakeslee, R. J., H. J. Christian, and B. Vonnegut (1989), Electrical measurements over thunderstorms, *J. Geophys. Res.*, 94, 135–140.

Boccippio, D. J., S. Heckman, and S. J. Goodman (2000a), A diagnostic analysis of the Kennedy Space Center LDAR network: 1. Data Characteristics, *J. Geophys. Res.*, 106, 4787–4796.

Boccippio, D. J., S. Heckman, and S. J. Goodman (2000b), A diagnostic analysis of the Kennedy Space Center LDAR network: 2. Cross sensor studies, *J. Geophys. Res.*, 106, 4769–4786.

Boyd, B. F., W. P. Roeder, D. L. Hajek, and M. B. Wilson (2005), Installation, upgrade and evaluation of a short baseline cloud-to-ground lightning surveillance system used to support space launch operations, Conf. on Meteorol. Applic. of Lightning Data, Amer. Meteorol. Soc. Annual Meeting, San Diego, Calif., 9–13 Jan.

Byrne, G. J., A. A. Few, and M. F. Stewart (1989), Electric field measurements within a severe thunderstorm anvil, *J. Geophys. Res.*, 94, 6297–6307.

Cummins, K. L., M. J. Murphy, E. A. Bardo, W. L. Hiscox, R. B. Pyle, and A. E. Pifer (1998), A combined TOA/MDF technology upgrade of the U.S. National Lightning Detection Network, *J. Geophys. Res.*, 103, 9035–9044.

Dye, J. E., and J. C. Willett (2007), Observed enhancement of reflectivity and electric field in long-lived Florida anvils, *Mon. Weather Rev.*, in press.

Dye, J. E., J. J. Jones, W. P. Winn, T. A. Cerni, B. Gardiner, D. Lamb, R. L. Pitter, J. Hallett, and C. P. R. Saunders (1986), Early electrification and precipitation development in a small, isolated Montana cumulonimbus, *J. Geophys. Res.*, 91, 1231–1247.

Dye, J. E., S. Lewis, M. G. Bateman, D. M. Mach, F. J. Merceret, J. G. Ward, and C. A. Grainger (2004), Final Report on the Airborne Field Mill Project (ABFM) 2000–2001 Field Campaign, NASA/TM-2004-211534, 132 pp., National Aeronautics and Space Administration, Kennedy Space Center, Fla. (Available from NASA Center for AeroSpace Information (CASI), 7121 Standard Drive, Hanover, Md 21076-1320)

Field, P. R., R. Wood, P. R. A. Brown, P. H. Kaye, E. Hirst, R. Greenaway, and J. A. Smith (2003), Ice particle interarrival times measured with a fast FSSP, *J. Atmos. Ocean. Technol.*, 20, 249–261.

Field, P. R., A. J. Heymsfield, and A. Bansemer (2006), Shattering and particle interarrival times measured by optical array probes in ice clouds, *J. Atmos. Ocean. Technol.*, 23, 1357–1371.

Heymsfield, A. J., and L. M. Milosevich (1989), Evaluation of liquid water measuring instruments during FIRE, *J. Atmos. Ocean. Technol.*, 6, 378–388.

Jayaratne, E. R., C. P. R. Saunders, and J. Hallett (1983), Laboratory studies of the charging of soft-hail during ice crystal interactions, *Q. J. R. Meteorol. Soc.*, 109, 609–630.

Klett, J. D. (1972), Charge screening layers around electrified clouds, *J. Geophys. Res.*, 77, 3187–3195.

Krider, E. P., H. C. Koons, R. L. Walterscheid, W. D. Rust, and J. C. Willett (1999), Natural and triggered lightning launch commit criteria (LCC), Aerospace Report No. TR-99(1413)-1, 15 pp., The Aerospace Corporation, El Segundo, Calif.

Lawson, R. P., R. E. Stewart, and L. J. Angus (1998), Observations and numerical simulations of the origin and development of very large snowflakes, *J. Atmos. Sci.*, 55, 3209–3229.

Lawson, P. R., B. A. Baker, C. G. Schmitt, and T. L. Jensen (2001), An overview of microphysical properties of Arctic clouds observed in May and July 1998 during FIRE, ACE, *J. Geophys. Res.*, 106, 14,989–15,014.

Lennon, C., and L. S. Maier (1991), Lightning mapping system, *Proceedings of the International Aerospace and Ground Conference on Lightning and Static Electricity*, pp. 89–91, Cocoa Beach, FL, 16–19 April 1991.

MacGorman, D. R., and W. D. Rust (1998), *The Electrical Nature of Storms*, 422 pp., Oxford Univ. Press, New York.

Mach, D. M., and W. J. Koshak (2003), General matrix inversion technique for the calibration of electric field sensor arrays on aircraft platforms, *Proceedings of the 12th International Conference on Atmospheric Electricity*, pp. 207–210, Versailles, France, 9–13 Jun.

Maier, M. W. (1991), Evaluation of 1990 bias error corrections for the ESMC cloud-to-ground lightning surveillance system, CSR-322-003, Eastern Space and Missile Center Report under Contract F08606-88-C-0014, Computer Sciences, Raytheon Corporation.

Marshall, T. C., W. D. Rust, and W. P. Winn (1984), Screening layers at the surface of thunderstorm anvils, *Proceedings of the VII International Conference on Atmospheric Electricity*, pp. 346–347, Albany, New York, 3–8 Jun.

Merceret, F. J., J. G. Ward, D. M. Mach, M. G. Bateman, and J. E. Dye (2007), On the magnitude of the electric field near thunderstorm-associated clouds, *J. Appl. Meteorol.*, in press.

Mohr, C. G., L. J. Miller, R. L. Vaughan, and H. W. Frank (1986), The merger of mesoscale data sets into a common Cartesian format for efficient and systematic analysis, *J. Atmos. Ocean. Technol.*, 3, 143–161.

Office of the Federal Coordinator for Meteorology (OFCM) (2003), *Federal Meteorological Handbook No. 11: Doppler Radar Observations, part A*, 34 pp.

Reiss, R.-D., and M. Thomas (2001), *Statistical Analysis of Extreme Values*, 2nd ed., 443 pp., Birkhauser Verlag, Boston, Mass.

Schild, S. J. (2003), Liquid water in thunderstorm anvils over Kennedy Space Center, Florida during the summer 2001 ABFM field campaign, master's thesis, 55, pp., Univ. of North Dakota.

Strapp, J. W., F. Albers, A. Reuter, A. V. Korolev, U. Maixner, E. Rashke, and Z. Vukovic (2001), Laboratory measurements of the response of a PMS OAP-2DC, *J. Atmos. Ocean. Technol.*, 18, 1150–1170.

Vonnegut, B., C. B. Moore, R. P. Espinola, and H. H. Blau Jr. (1966), Electric potential gradients above thunderstorms, *J. Atmos. Sci.*, 23, 764–770.

Ward, J. L., F. J. Merceret, and C. A. Grainger (2003), An automated cloud-edge detection algorithm using cloud physics and radar data, NASA/TM-2003-211189, 20 pp., National Aeronautics and Space Administration, Kennedy Space Center, Fla. (Available from NASA Center for Aero-Space Information (CASI), 7121 Standard Drive, Hanover, Md 21076-1320).

Wheeler, M. W. (1997), Report on the Radar/PIREP Cloud Top Discrepancy Study, NASA Kennedy Space Center FL, Contractor Report CR-204381, 18 pp.

Willett, J. C., and J. E. Dye (2003), A simple model to estimate electrical decay times in anvils, *Proceedings of the 12th International Conference on Atmospheric Electricity*, pp. 267–271, Versailles, France, Jun 2003.

Willett, J. C., D. A. Davis, and P. Laroche (1999), An experimental study of positive leaders initiating rocket-triggered lightning, *Atmos. Res.*, 51, 189–219.

Winn, W. P., C. B. Moore, C. R. Holmes, and L. G. Byerley (1978), Thunderstorm on July 16, 1975 over Langmuir Laboratory: A case study, *J. Geophys. Res.*, 83, 3079–3092.

————————————

M. G. Bateman, Universities Space Research Association, Huntsville, AL, USA.

H. J. Christian and D. M. Mach, University of Alabama in Huntsville, Huntsville, AL, USA.

E. Defer, Observatoire de Paris, Paris, France.

J. E. Dye, 3450 Mitchell Lane, FL3, Boulder, CO 80307-3000, USA. (dye@ucar.edu)

C. A. Grainger, University of North Dakota, Grand Forks, ND, USA.

W. D. Hall, National Center for Atmospheric Research, PO Box 3000, Boulder, CO 80307-3000, USA.

E. P. Krider, University of Arizona, Tucson, AZ, USA.

S. A. Lewis, NOAA/University of Colorado, Cooperative Institute for Research in Environmental Sciences, Boulder, CO, USA.

F. J. Merceret, National Aeronautics and Space Administration, Kennedy Space Center, FL, USA.

J. C. Willett, Garrett Park, MD, USA.

P. T. Willis, NOAA Cooperative Institute for Marine and Atmospheric Sciences, Miami, FL, USA.